Scripta Materialia 225 (2023) 115165

Contents lists available at ScienceDirect

Scripta Materialia

journal homepage: www.journals.elsevier.com/scripta-materialia

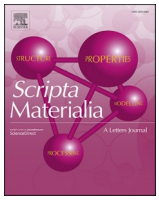

Formation of a protective oxide layer with enhanced wear and corrosion resistance by heating the $TiZrHfNbFe_{0.5}$ refractory multi-principal element alloy at 1,000 °C

Nengbin Hua [a,c,*], Zhongya Qian [a,c], Bozhuan Lin [a,c], Zhenlong Liao [b], Qianting Wang [a,c], Pinqiang Dai [a,c], Hui Fang [a,c], Peter K. Liaw [d]

[a] Department of Materials Science and Engineering, Fujian University of Technology, 350118 Fuzhou, China
[b] Department of Materials Science and Engineering, Beihang University, 100191 Beijing, China
[c] Fujian Provincial Key Laboratory of Advanced Materials Processing and Application, Fujian University of Technology, 350118 Fuzhou, China
[d] Department of Materials Science and Engineering, The University of Tennessee, 37996–2200 Knoxville, TN, USA

ARTICLE INFO

Keywords:
Metallic biomaterials
Refractory multi-principal element alloy
Wear resistance
Corrosion resistance
Bioactivity

ABSTRACT

In the present work, the effects of oxidation treatment on the structures and properties of a novel $TiZrHfNbFe_{0.5}$ refractory multi-principal element alloy (MPEA) were reported. It is found that the $TiZrHfNbFe_{0.5}$ MPEA exhibits a sluggish oxidation rate at 1,000 °C, which is attributed to the formation of a compact and stable oxide layer consisting of complex metallic oxides like Ti_2ZrO_6 and Fe_2O_3. In comparison with the as-cast MPEA, the microhardness of the 1,000 °C oxidized MPEA significantly increases by 1.6 times, resulting in a two orders of magnitude higher wear resistance. Furthermore, the bio-corrosion resistance, hydrophilicity, and bioactivity of the MPEA are remarkably enhanced by the 1,000 °C oxidation. In short, the formation of a highly protective oxide layer with enhanced wear and corrosion resistance by heating the $TiZrHfNbFe_{0.5}$ MPEA at 1,000 °C, which shows promising prospects for biomedical applications.

Owing to their good bio-corrosion and mechanical performances, titanium alloys have been widely employed in the application of orthopedic-implantation [1,2]. However, current implant titanium alloys, e.g., Ti6Al4V, still encounter several complexities in clinical service. For instance, titanium alloys exhibit a much higher elastic modulus of 110 GPa than that of human bones of 10 - 40 GPa, resulting in the stress-shielding effect [3]. Moreover, the elemental Al of the Ti6Al4V alloy may cause Alzheimer's disease, and the elemental V has a high biological toxicity and may cause cancer [4]. Furthermore, due to the poor wear resistance of titanium alloys, wear products may induce inflammation and cause aseptic loosening [5]. In addition, titanium alloys are generally bioinert, which prevents them forming an active bond with human bones [2,3].

High-entropy alloys (HEAs) are composed of at least five principal elements, which exhibit a nominally single-phase structure and excellent performances [6,7]. In fact, more broadly alloy systems, termed multi-principal element alloys (MPEAs) have in many instances also demonstrated unique properties [6]. Among various MPEAs systems, TiZr-transition group metal refractory MPEAs, such as Ti-Zr-Hf-Nb [8], Ti-Nb-Ta-Zr [9], Ti-Nb-Ta-Zr-Mo [10–12], Ti-Nb-Ta-Zr-Hf [13–18], Ti-Nb-Zr-Hf-Mo [19], Ti-Zr-Hf-Nb-Fe [20] et al., display a variety of properties superior to those of traditional biomedical metallic materials. For instance, the TiNbTaZrHf MPEA is composed of the body-centered-cubic (BCC) phase and tiny HCP phase and display a lower elastic modulus of 78 GPa than that of the Ti6Al4V alloy, which weakens the stress-shielding effect [15]. Furthermore, due to the low biotoxicity of constituent elements, such as Ti, Zr, Hf, Nb, Ta, and Mo, refractory MPEAs show low cell cytotoxicity, high cell adsorption and proliferation ability, and thus good biocompatibility [4,15,17]. As a result, the refractory MPEAs exhibit promising application potential as biomedical-implant materials.

Although the wear performance of the refractory MPEAs reported so far is mostly superior to that of Ti6Al4V alloy, it is still significantly inferior to that of well-known biomedical alloys of the 316 L stainless steel and CoCrMo alloy [12,20]. Furthermore, the bioinert nature of the refractory MPEAs should be improved when they are used as implant

* Corresponding author at: Nengbin Hua, who will handle the correspondence at all stages of paper reviews, publication, and post-publication. School of Materials Science and Engineering, Fujian University of Technology, Fuzhou 350118, China
E-mail address: flower1982cn@126.com (N. Hua).

https://doi.org/10.1016/j.scriptamat.2022.115165
Received 11 September 2022; Received in revised form 10 November 2022; Accepted 10 November 2022
Available online 16 November 2022

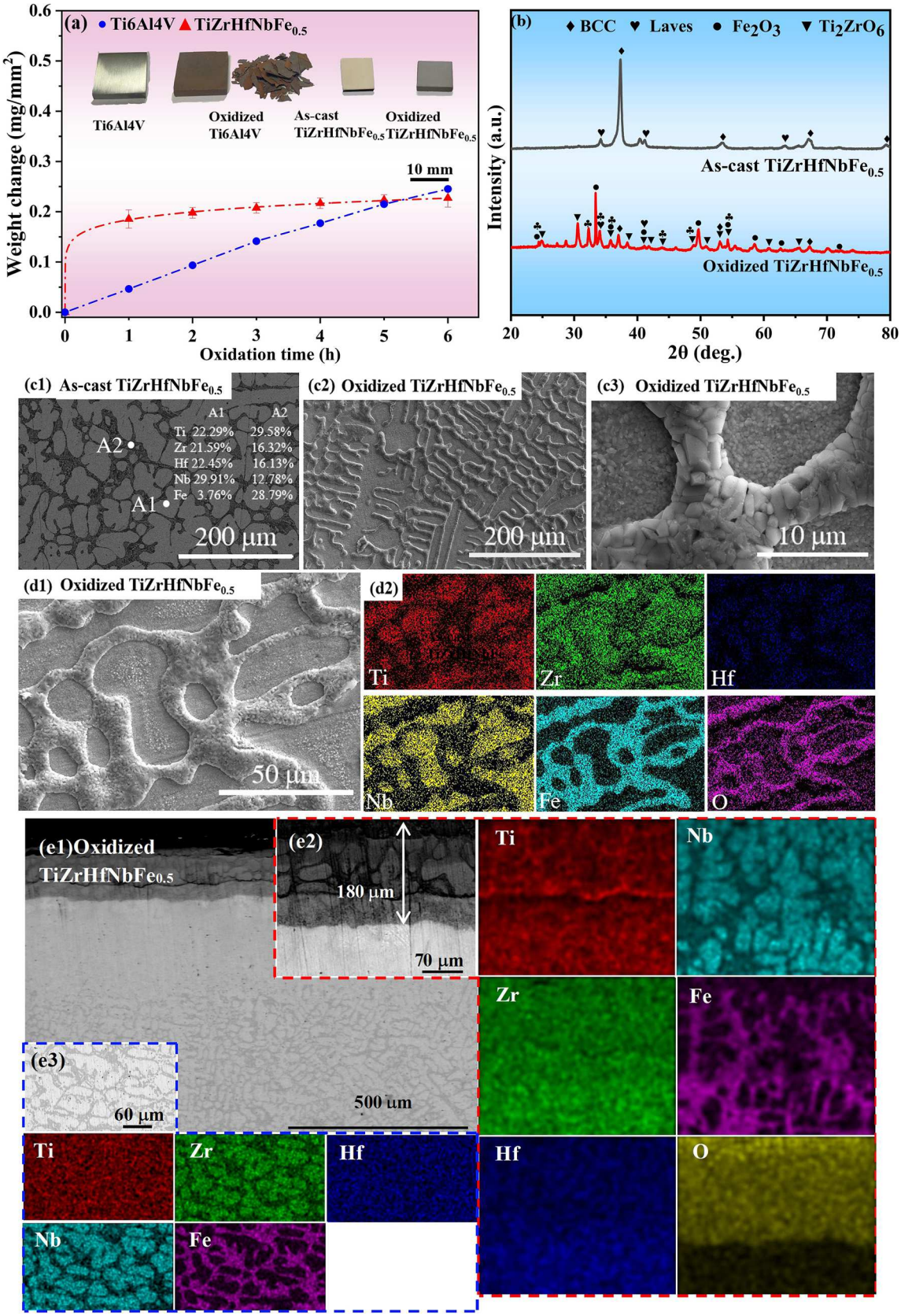

Fig. 1. (a) Weight gain per unit area of the $TiZrHfNbFe_{0.5}$ MPEA as a function of heating time under the oxidation temperature of 1000 °C. (b) XRD patterns of the as-cast and 1000 °C-oxidized $TiZrHfNbFe_{0.5}$ MPEAs. (c1) Backscattered electron SEM image of the surface morphology for the as-cast $TiZrHfNbFe_{0.5}$ MPEA. (c2-c3) SEM images of surface morphologies for the 1000 °C-oxidized $TiZrHfNbFe_{0.5}$ MPEA. (e1) Cross-sectional backscattered electron SEM morphology, and corresponding EDS mapping of the (e2) oxide layer and (e3) inner matrix regions of the 1000 °C-oxidized $TiZrHfNbFe_{0.5}$ MPEA.

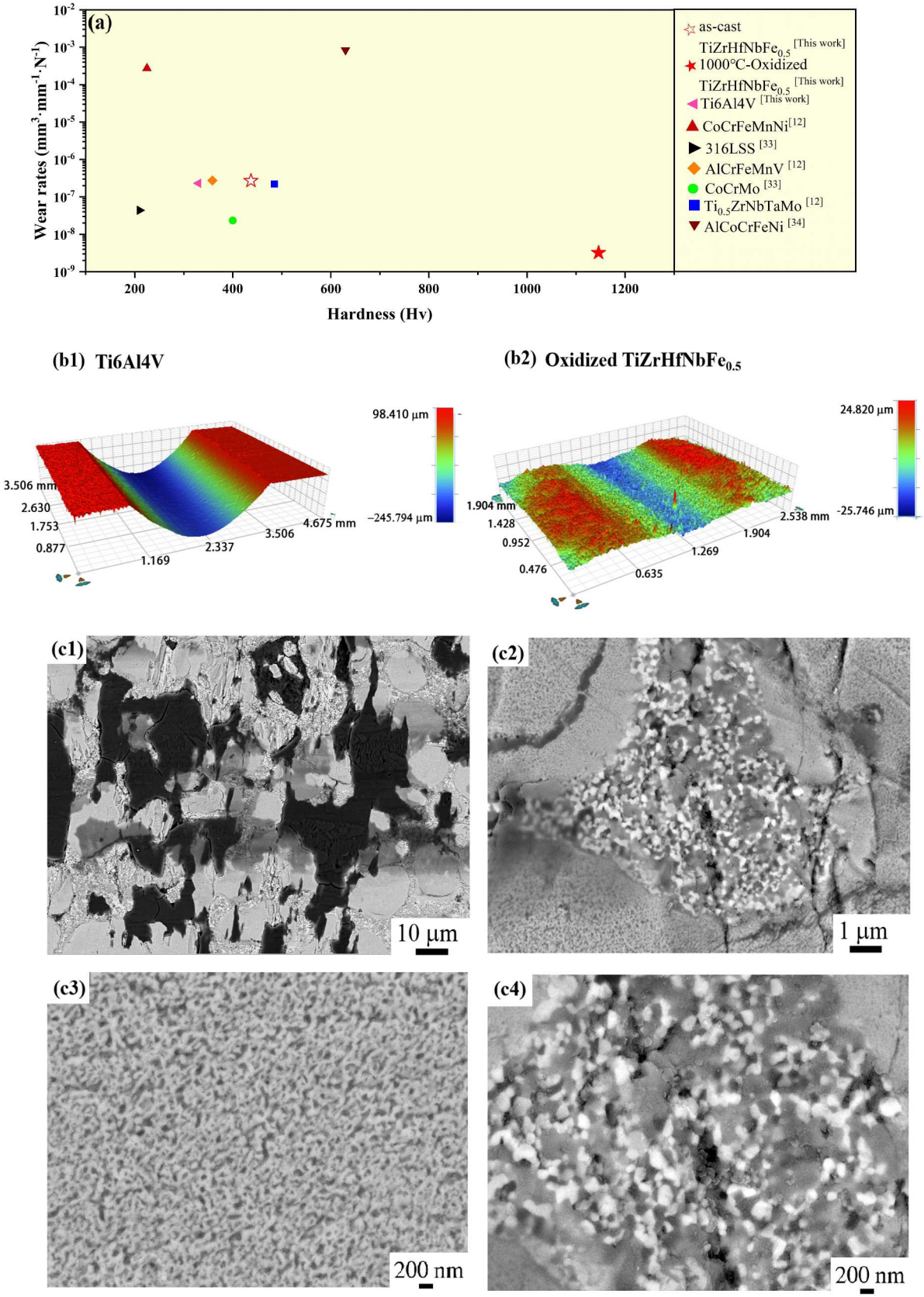

Fig. 2. (a) Wear rates and hardness of various MPEAs and the conventional biometals. Three-dimensional morphologies of the (b1) Ti6Al4V alloy and (b2) 1000 °C-oxidized $TiZrHfNbFe_{0.5}$ MPEAs. (c1-c4) SEM morphologies of worn scars for the 1000 °C-oxidized MPEA.

materials. To improve surface performances, various surface-treatment technologies, including the oxidation heat treatment [21], nitriding [22], micro-arc oxidation [23], ion implantation [24], physical vapor deposition [25], and laser cladding [26], have been performed on titanium alloys. Among those, the oxidation heat treatment is characterized by the simple process, low cost, and large film thickness, and thus, exhibit a promising application prospect. Nevertheless, investigations on the oxidation treatment of TiZr-based refractory MPEAs to improve their performance for biomedical applications have not yet been reported to date.

In our previous work, a new $TiZrHfNbFe_{0.5}$ refractory MPEA was developed, which shows a relatively low Young's modulus of 50 GPa, high strength of 1450 MPa, and distinct plasticity [20]. Moreover, the refractory MPEA is corrosion-resistant in a phosphate buffer saline (PBS) solution [20]. In the present study, a compact and stable layer with complex metallic oxides was obtained on the $TiZrHfNbFe_{0.5}$ MPEA after being oxidized at 1000 °C for 6 h. The hardness, wear resistance, bio-corrosion resistance, and surface bioactivity of the MPEA were significantly improved, which effectively promotes the application of MPEA in the field of biomedical-implant alloys.

Pure metals with a purity of above 99.5 wt percent (wt.%) were arc-melted for at least 4 times to fabricate master alloys with a composition of $TiZrHfNbFe_{0.5}$ (in a molar ratio) on a water-cooled copper crucible under a high-purity argon atmosphere. Rectangular-plate samples with a gage of $10 \times 10 \times 2$ mm^3 were machined from the central part of master alloys, ground with diamond sandpapers, and then polished. The alloy samples were heated in the atmosphere at 1000 °C for 6 h. The weight gain of the MPEA was measured for each hour by an electronic balance with a high precision of 0.0001 g. The structures of the as-cast and oxidized MPEAs were examined by an X-ray diffractometer (XRD, D8 advance). The surface morphologies and compositions of samples were analyzed by scanning electron microscopy (SEM, Nova nano SEM 450) with an X-ray energy spectrum (EDS).

The micro-hardness test was performed by a THV-10D Vickers hardness tester using a load of 300 gf and a dwell time of 15 s. The reciprocating sliding tests were carried out by an MSR-2T tribometer, employing a Si_3N_4 couple pair ball. The wear volume (ΔW) of MPEAs was measured by a GT-X 3D surface profilometer. The wear rate (W_S) of samples is calculated, according to the formula: $\Delta W = W_S / (S{\cdot}N)$, where N is the applied normal load, and S is the friction distance. SEM and EDS were employed to analyze the morphology and composition of wear scars.

The potentiodynamic-polarization curves of samples in the phosphate buffer saline (PBS) solution were examined by a PGSTAT 302 N electrochemical workstation. The surface chemistry of RHEAs was analyzed by the ESCALab250Xi X-ray photoelectron spectroscopy (XPS). The contact angle and surface-free energy (SFE) of alloys were measured by a DSA 25 CAM-Plus contact angle meter. To evaluate the bioactivity of the 1000 °C-oxidized MPEA, the surfaces of alloy samples were immersed in a simulated body fluid (SBF) for 14 days, and then examined by SEM and EDS. The components of the PBS and SBF solutions can be found in references [12,27].

Fig. 1(a) shows the weight gain per unit area of the $TiZrHfNbFe_{0.5}$ MPEA as a function of the heating time under the oxidation temperature of 1000 °C, using a Ti6Al4V alloy as a reference sample. The insets present the morphology images of the as-cast and 1000 °C-oxidized alloy samples. The weight gain of the Ti6Al4V alloy nearly linearly increases as the heating time prolongs. Spall-off fragments of the oxidation layer can be observed for the Ti6Al4V alloy after being heated at 1000 °C. The weight gain of the MPEA promptly increases at the initial 1 h of oxidation and then remains almost steady as the oxidation time prolongs, exhibiting a sluggish oxidation behavior. It is visible that a consecutive oxide layer in silver gray is formed on the surface of the MPEA after being heated at 1000 °C.

Fig. 1(b) displays the XRD patterns of the as-cast and 1000 °C-oxidized $TiZrHfNbFe_{0.5}$ MPEAs. The as-cast MPEA consists of the BCC and Laves phases. After the oxidation treatment at 1000 °C, an oxide layer, including Ti_2ZrO_6 and Fe_2O_3, is formed on the alloy surface. It has been reported that titanium alloys are usually oxidized at 600 ~ 800 °C to obtain a TiO_2-surface film. Unfortunately, during the long-time oxidation process at high heating temperatures, the oxide film is easy to delaminate, which results from the localized stress [28,29]. Owing to the characteristics of multi-principal elements and the simple solid-solution structure, the formation of Ti_2ZrO_6 ($2TiO_2{\cdot}ZrO_2$) can occur due to TiO_2 reacting with ZrO_2 [30]. It was found that the thick Ti_2ZrO_6 layer was intact and protective, which led to the sluggish oxidation kinetics and acted as the barrier layer [30].

Fig. 1(c1) presents the backscattered-electron SEM image of the surface morphology for the as-cast $TiZrHfNbFe_{0.5}$ MPEA. The as-cast MPEA is composed of the bright-contrast dendrite (DE) and dark-contrast interdendrite (ID) regions. The inset of Fig. 1(c1) lists the EDS results on typical sites of DE and ID regions. It is seen that there are Ti, Zr, Hf, Nb, and Fe elements in both DE and ID regions. Nevertheless, the enriched Nb and depleted Fe is found in the DE region, whereas the Fe is enriched, and Nb is depleted in the ID region.

Figs. 1(c2-c3) depict the SEM images of surface morphologies for the 1000 °C-oxidized $TiZrHfNbFe_{0.5}$ MPEA. It is visible that the connected island-shaped oxidation products with a width of about 10 μm formed on the alloy surface. The island-shaped oxidation products consist of a variety of closely accumulating particles with a size of 1 ~ 2 μm. Meanwhile, nano-sized particles are homogeneously and compactly distributed on the relatively flat area around the island-shaped convex. Combined with the EDS mapping [Fig. 1(d2)] and XRD analysis results [Fig. 1(b)], it is illustrated that the island-shaped convex region with a high fraction of Fe and O is mainly composed of Fe_2O_3 grains, which locates above the ID region enriching in the elemental Fe. The flat area merely consists of nano-sized Ti_2ZrO_6 oxide particles, which corresponds to the DE region. The surface morphology image of the 1000 °C-oxidized Ti6Al4V alloy (not shown here) that there are a large amount of pores on the oxide layer, which provides several channels for oxygen passing through and results in the linear oxidation kinetics.

The grain size of Fe_2O_3 is obviously larger than that of Ti_2ZrO_6, which is related to the oxidation rate of different constituent components. According to the Wagner's parabolic oxidation theory, the parabolic oxidation rate constant, K_w, of metallic oxides correlates to the oxidation velocity and does not necessarily related to the stability of the corresponding metallic oxides [31]. Although the TiO_2 is thermodynamic stabler than Fe_2O_3, the K_w of TiO_2 is one order of magnitude smaller than that of Fe_2O_3 [32]. For the Fe-rich phase, the fraction of Fe ions diffusing through the metallic oxide layer is lager than that of the Fe-depleted phase. Owing to the high K_w of Fe_2O_3, the oxidation rate of thickness of the Fe_2O_3 oxide layer is significantly larger than that of Ti_2ZrO_6, resulting in the formation of island-shaped convex.

Figs. 1(e1) present the cross-sectional backscattered-electron SEM morphology of the 1000 °C-oxidized $TiZrHfNbFe_{0.5}$ MPEA. Figs. 1(e2) and 1(e3) display the EDS mapping of the oxide layer and inner matrix regions. The oxide layer on the MPEA surface has a thickness of about 180 μm with a distinct higher fraction of oxygen than that of the region below the oxide layer [Fig. 1(e2)]. It can be seen that there is dual phase structure in the core area of the annealed MPEA, which is almost identical with that of the as-cast alloy [Fig. 1(e3)].

Fig. 2(a) summarizes the wear rate and hardness of various MPEAs and the conventional biometals. The microhardness enhances from 440 HV for the as-cast RHEA to 1146 HV for the 1000 °C-oxidized MPEA. The wear rate of the Ti6Al4V alloy is 2.4×10^{-7} $mm^3{\cdot}mm^{-1}{\cdot}N^{-1}$, which is two orders of magnitude larger than that of 3.23×10^{-9} $mm^3{\cdot}mm^{-1}{\cdot}N^{-1}$ for the 1000 °C-oxidized MPEA. The wear resistance of the oxidized $TiZrHfNbFe_{0.5}$ MPEA is significantly higher than that of the other MPEAs and the Ti6Al4V, 316 L stainless steel, and CoCrMo alloys [12,17-20,33,34], which implies that the oxidized MPEA is promising in the application of high wear-resistant implantation instruments.

Figs. 2(b1-b2) present the three-dimensional morphologies of the

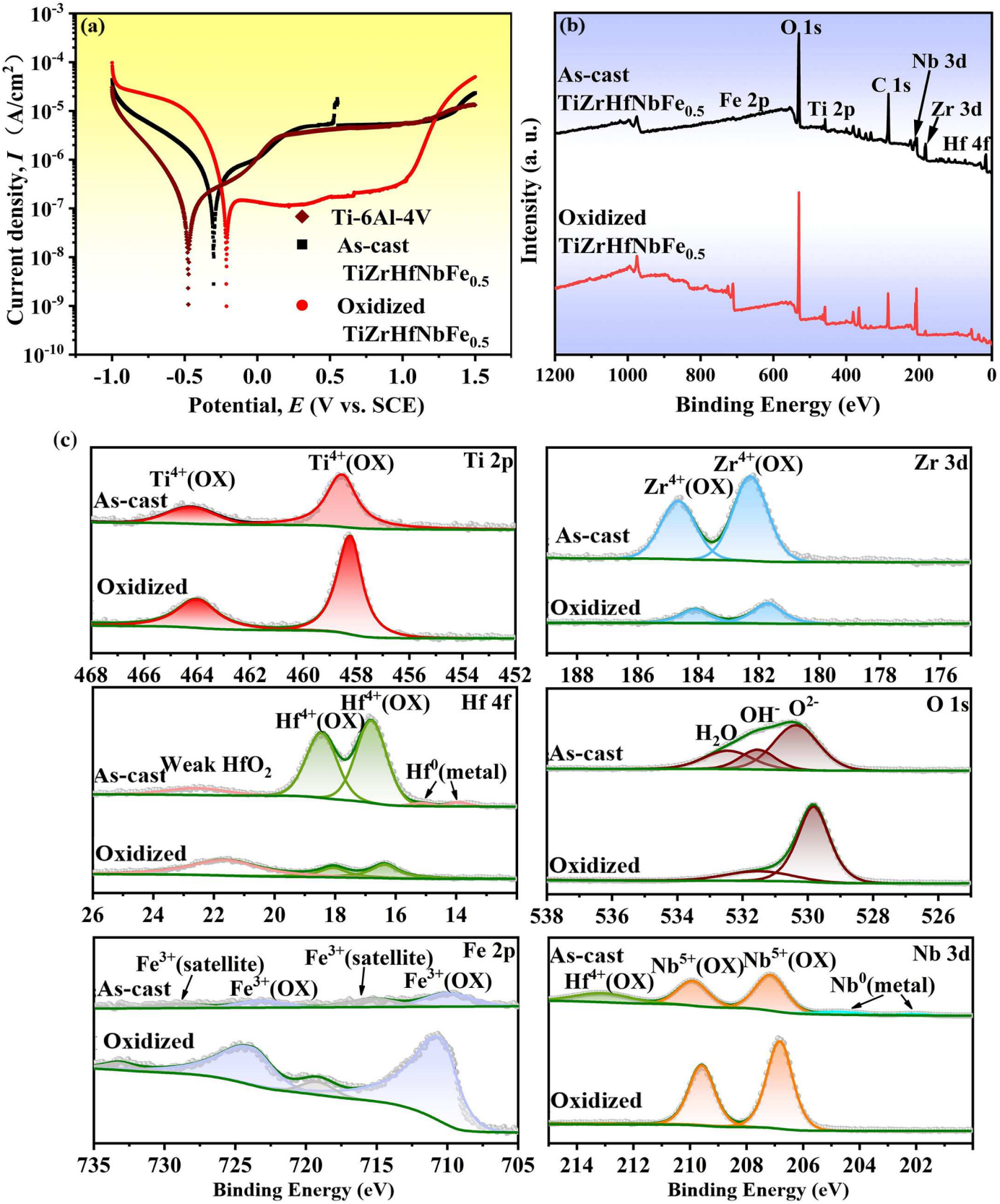

Fig. 3. (a) Potentiodynamic-polarization curves of the as-cast and oxidized $TiZrHfNbFe_{0.5}$ MPEAs as well as the Ti6Al4V alloy in the PBS solution. (b) Full spectrum and (c) narrow scanning spectra of constituent elements for the as-cast and oxidized $TiZrHfNbFe_{0.5}$ MPEAs.

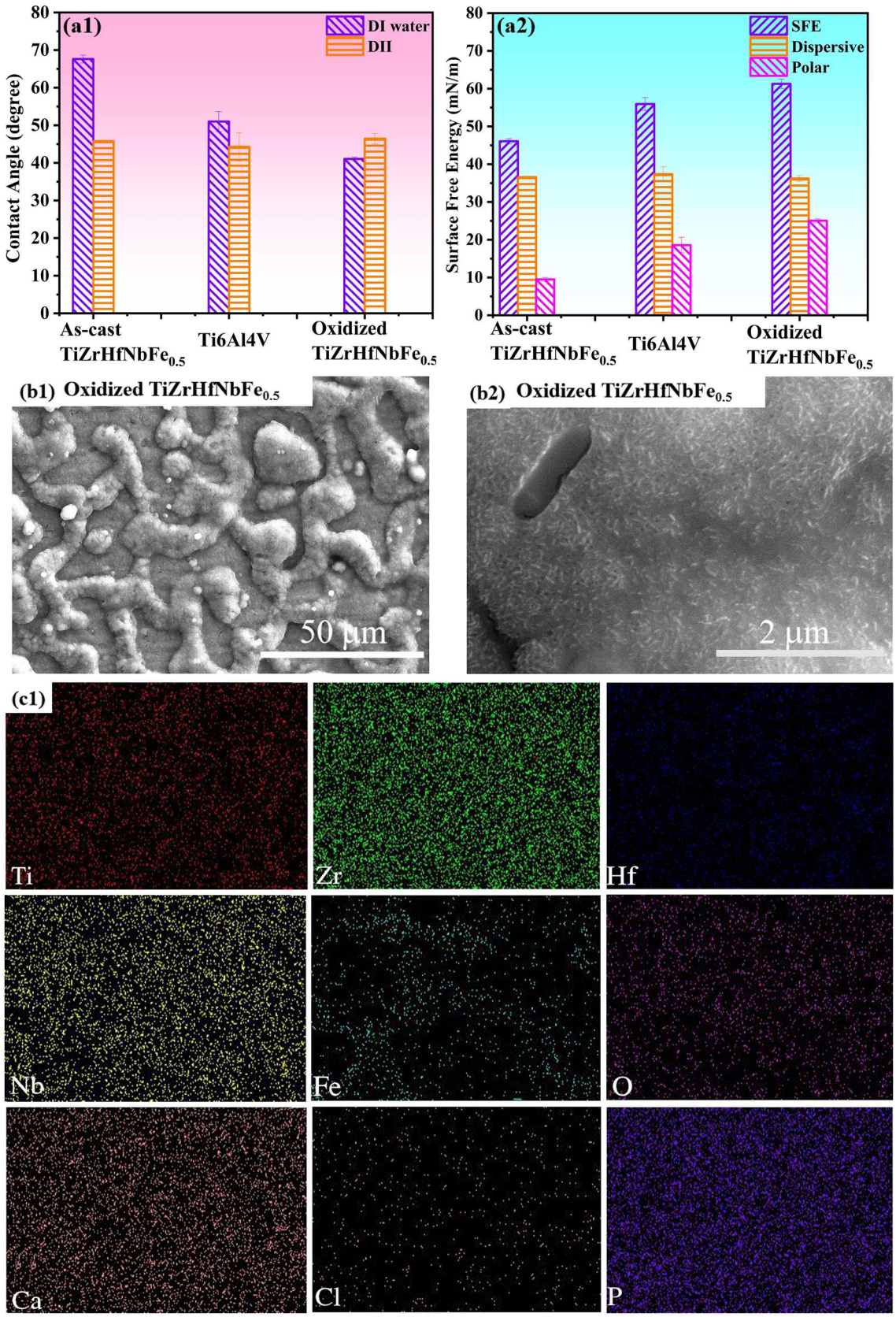

Fig. 4. (a1) Contact angle and (a2) surface free energy (SFE) of the deionized water (DI) and diiodomethane (DII) on the surfaces of the as-cast and 1000 °C-oxidized $TiZrHfNbFe_{0.5}$ MPEAs. (b1-b2) SEM images of the surface morphologies of the 1000 °C-oxidized $TiZrHfNbFe_{0.5}$ MPEAs, immersed in a simulated body fluid (SBF) at 37 °C for 14 days. (c) EDS mapping of the constituent elements from Fig. 4(b1).

Ti6Al4V alloy and 1000 °C-oxidized $TiZrHfNbFe_{0.5}$ MPEA, respectively. There is a deep and wide wear scar on the surface of the Ti6Al4V alloy after the reciprocating friction for 5 h. However, the wear scar surface of the 1000 °C-oxidized MPEA is relatively flat with only slight scratches, indicating the excellent wear resistance of the oxidized MPEA. Figs. 2 (c1-c4) exhibit the SEM morphologies of worn scars for the 1000 °C-oxidized MPEA. It can be seen from Fig. 2(c1) that the Si_3N_4 ball debris was dispersed in the worn scar of the oxidized MPEA, which further confirms its high wear resistance. Figs. 2(c2-c4) demonstrate that the island-shaped convex region is worn down, and the μm-sized Fe_2O_3 grains are ground to ~ 100 nm-sized grains, which has been reported to be beneficial to forming a lubricating tribolayer and improving the wear resistance [35]. Moreover, the flat area consisted of nano-sized Ti_2ZrO_6 particles shows scarcely any sign of wear and tear, which indicates that the high wear resistance mainly results from the compact and stable nanostructured oxide layer.

The potentiodynamic-polarization curves of the as-cast and oxidized $TiZrHfNbFe_{0.5}$ MPEAs as well as the Ti6Al4V alloy in the PBS solution are presented in Fig. 3(a). The corrosion potentials of the as-cast and oxidized MPEAs are higher than that of the Ti6Al4V alloy. The oxidized MPEA exhibits the highest corrosion potential of - 0.21 V, indicating the formation of the highly stable passive film in the PBS solution. Moreover, the oxidized MPEA displays the lowest corrosion current density and passivation current density, demonstrating the superior corrosion resistance among all alloy samples.

Figs. 3(b-c) display the full spectrum and narrow scanning spectra of constituent elements for the as-cast and oxidized $TiZrHfNbFe_{0.5}$ MPEAs, respectively. It is seen in Fig. 3(b) that the peaks of Ti 2p, Zr 3d, Hf 4f, Nb 3d, Fe 2p, C 1 s, and O 1 s are detected in the full spectrum for both as-cast and oxidized MPEAs. The O on the surface of the as-cast MPEA is mainly in terms of O^{2-}, OH^-, and bound water (H_2O). Due to the oxidation at 1000 °C, the O on the surface of the oxidized MPEA turns into chiefly the O^{2-}. From the narrow scanning spectra of Ti 2p, Zr 3d, Hf 4f, Nb 3d, Fe 2p, and O 1 s in Fig. 3(c), it can be found that the fractions of Zr^{4+} and Hf^{4+} are reduced, and Ti^{4+}, Nb^{5+}, Fe^{3+}, and O^{2-} on the oxidized MPEA are significantly enriched in comparison with those of the as-cast MPEA. The existence of the highly-protective nano-structured Ti_2ZrO_6 on the oxidized MPEA surface contributes to the enhanced corrosion resistance.

Figs. 4(a1-a2) illustrate the contact angle and surface free energy (SFE) of the deionized water (DI) and diiodomethane (DII) on the surface of the as-cast and 1000 °C-oxidized $TiZrHfNbFe_{0.5}$ MPEAs as well as the Ti6Al4V alloy, respectively. It is noted that the oxidized MPEA exhibits the lowest water contact angle of about 40° and the highest surface energy up to 61.29 mN/m. Previous reports demonstrated that when the water contact angle is less than the Berg limit ($\theta = 65°$) or the SFE value exceeds 50 mN/m, the surface of materials exhibits good hydrophilicity, which is conducive to cell adhesion and growth, and thus results in good biocompatibility [36].

Figs. 4(b1-b2) show the SEM images of the surface morphologies of the 1000 °C-oxidized $TiZrHfNbFe_{0.5}$ MPEA, immersed in a simulated body fluid (SBF) at 37 °C for 14 days. A compact and intact reaction product layer is found, covering on the whole surface of the oxidized MPEA. The high-magnification SEM image on the island-shaped Fe-oxides convex in Fig. 4(b2) demonstrates that a great number of nano-sized needle-like precipitation products filled in the glaze-like reaction layer. The EDS mapping of the constituent elements is listed in Fig. 4(c). It is discovered that Ca and P are found on the surface of the oxidized MPEA, which corresponds to the formation of the hydroxyapatite. The great hydroxyapatite-forming ability of the oxidized MPEA further indicates its good bioactivity and preliminary biocompatibility.

In conclusion, the microstructures and properties of the surface oxide layer for the $TiZrHfNbFe_{0.5}$ MPEA heated at the temperature of 1000 °C were investigated. The MPEA exhibits a sluggish oxidation behavior at 1000 °C owing to the formation of the complex metallic oxide on the alloy surface, which consists of Ti_2ZrO_6 and Fe_2O_3. The complex metallic oxide layer has a compact and stable structure, which remarkably improve the hardness, wear and corrosion resistance, as well as surface bioactivity of the MPEA. In short, the highly-protective oxide layer forming on the surface of the $TiZrHfNbFe_{0.5}$ MPEA by heating at 1000 °C offers a novel strategy to fabricate materials or coating with excellent corrosion and wear resistance.

Data availability

The raw/processed data required to reproduce these findings cannot be shared at this time as the data also forms part of an ongoing study.

Declaration of Competing Interest

The authors declare that they have no known competing financial interests or personal relationships that could have appeared to influence the work reported in this paper.

Acknowledgement

The present work was supported by the Scientific Research Project of the Fujian Provincial Department of Science and Technology (2021H0023 and 2022L3062), and the Scientific Research Project of the Fujian University of Technology (GY-Z21032 and GY-Z20057). P.K. Liaw also acknowledges the support from the National Science Foundation under grant DMR-1611180 and 1809640.

References

[1] Q.Z. Chen, G.A. Thouas, Metallic implant biomaterials, Mater. Sci. Eng. R 87 (2015) 1–57.
[2] M. Geetha, A.K. Singh, R. Asokamani, A.K. Gogia, Ti based biomaterials, the ultimate choice for orthopaedic implants - a review, Prog. Mater. Sci. 54 (2009) 397–425.
[3] M. Long, H.J.B. Rack, Titanium alloys in total joint replacement - a materials science perspective, Biomaterials 19 (1998) 1621–1639.
[4] M. Niinomi, Recent metallic materials for biomedical applications, Metall. Mater. Trans. A 33A (2002) 477–485.
[5] M.Z. Ibrahim, A.A.D. Sarhan, F. Yusuf, M. Hamdi, Biomedical materials and techniques to improve the tribological, mechanical and biomedical properties of orthopedic implants - a review article, J. Alloys Compd. 714 (2017) 636–667.
[6] N. Birbilis, S. Choudhary, J.R. Scully, M.L. Taheri, A perspective on corrosion of multi-principal element alloys, NPJ Mat. Degrad. 5 (2021) 14.
[7] D.B. Miracle, O.N. Senkov, A critical review of high entropy alloys and related concepts, Acta Mater 122 (2017) 448–511.
[8] Y.D. Wu, Y.H. Cai, T. Wang, J.J. Si, J. Zhu, Y.D. Wang, X.D. Hui, A refractory $Hf_{25}Nb_{25}Ti_{25}Zr_{25}$ high-entropy alloy with excellent structural stability and tensile properties, Mater. Lett. 130 (2014) 277–280.
[9] V.T. Nguyen, M. Qian, Z. Shi, T. Song, L. Huang, J. Zou, A novel quaternary equiatomic Ti-Zr-Nb-Ta medium entropy alloy (MEA), Intermetallics 101 (2018) 39–43.
[10] M. Todai, T. Nagase, T. Hori, A. Matsugaki, A. Sekita, T. Nakano, Novel TiNbTaZrMo high-entropy alloys for metallic biomaterials, Scr. Mater. 129 (2017) 65–68.
[11] S.P. Wang, J. Xu, TiZrNbTaMo high-entropy alloy designed for orthopedic implants: as-cast microstructure and mechanical properties, Mater. Sci. Eng. C 73 (2017) 80–89.
[12] N.B. Hua, W.J. Wang, Q.T. Wang, Y.X. Ye, S.H. Lin, L. Zhang, Q.H. Guo, J. Brechtl, P.K. Liaw, Mechanical, corrosion, and wear properties of biomedical Ti-Zr-Nb-Ta-Mo high entropy alloys, J. Alloys Compd. 861 (2021), 157997.
[13] Y. Yuan, Y. Wu, Z. Yang, X. Liang, Z.F. Lei, H.L. Huang, H. Wang, X.J. Liu, K. An, W. Wu, Z.P. Lu, Formation, structure and properties of biocompatible TiZrHfNbTa high entropy alloys, Mater. Res. Lett 7 (2019) 225–231.
[14] A. Motallebzadeh, N.S. Peighambardoust, S. Sheikh, H. Murakami, S. Guo, D. Canadinc, Microstructural, mechanical and electrochemical characterization of TiZrTaHfNb and $Ti_{1.5}ZrTa_{0.5}Hf_{0.5}Nb_{0.5}$ refractory high-entropy alloys for biomedical applications, Intermetallics 113 (2019), 106572.
[15] W. Yang, Y. Liu, S.J. Pang, P.K. Liaw, T. Zhang, Bio-corrosion behavior and in vitro biocompatibility of equimolar TiZrHfNbTa high-entropy alloy, Intermetallics 124 (2020), 106845.
[16] Q. Zhou, S. Sheikh, P. Ou, D. Chen, Q. Hu, S. Guo, Corrosion behavior of $Hf_{0.5}Nb_{0.5}Ta_{0.5}Ti_{1.5}Zr$ refractory high-entropy alloy in aqueous chloride solutions, Electrochem. Commun. 98 (2019) 63–68.
[17] W. Yang, S.J. Pang, Y. Liu, Q. Wang, P.K. Liaw, T. Zhang, Design and properties of novel Ti-Zr-Hf-Nb-Ta high-entropy alloys for biomedical applications, Intermetallics 141 (2022), 107421.

[18] V. Bhardwaj, Q. Zhou, F. Zhang, W. Han, Y. Du, K. Hua, H. Wang, Effect of Al addition on the microstructure, mechanical and wear properties of TiZrNbHf refractory high entropy alloys, Tribol. Int. 160 (2021), 107031.
[19] N.N. Guo, L. Wang, L.S. Luo, X.Z. Li, Y.Q. Su, J.J. Guo, H.Z. Fu, Microstructure and mechanical properties of refractory MoNbHfZrTi high-entropy alloy, Mater. Des. 81 (2015) 87–94.
[20] W.J. Wang, K.H. Yang, Q.T. Wang, P.Q. Dai, H. Fang, F.J. Wu, Q.H. Guo, P.K. Liaw, N.B. Hua, Novel Ti-Zr-Hf-Nb-Fe refractory high-entropy alloys for potential biomedical applications, J. Alloys Compd. 906 (2022), 164383.
[21] B.Z. Lin, K.H. Yang, X.G. Bao, J.L. Liu, Q.H. Guo, L. Zhang, Q.T. Wang, N.B. Hua, Enhanced wear, corrosion, and corrosive-wear resistance of the biocompatible Ti-based bulk metallic glass by oxidation treatment, J. Non-Cryst. Solids 576 (2022), 121231.
[22] F.A.P. Fernandes, S.C. Heck, C.A. Picone, L.C. Casteletti, On the wear and corrosion of plasma nitrided AISI H13, Surf. Coat. Technol. 381 (2020), 125216.
[23] X.Q. Shi, W. Yang, Z.H. Cheng, W.T. Shao, D.P. Xu, Y. Zhang, J. Chen, Influence of micro arc oxidation on high temperature oxidation resistance of AlTiCrVZr refractory high entropy alloy, Int. J. Refract. Met. H. 98 (2021), 105562.
[24] I. Vazirgiantzikis, S.L. George, L. Pichon, Surface characterisation and silver release from Ti-6Al-4V and anodic TiO_2 after surface modification by ion implantation, Surf. Coat. Technol. 433 (2022), 128115.
[25] P. Trivedi, P. Gupta, S. Srivastava, R. Jayaganthan, R. Chandra, P. Roy, Characterization and in vitro biocompatibility study of Ti-Si-N nanocomposite coatings developed by using physical vapor deposition, Appl. Surf. Sci. 293 (2014) 143–150.
[26] H. Raghuram, C. Katsich, K. Pichelbauer, K. Koschatzky, C. Gachot, U. Cihak-Bayr, Design of wear and corrosion resistant FeNi-graphite composites by laser cladding, Surf. Coat. Technol. 377 (2019), 124897.
[27] T. Kokubo, Bioactive glass ceramics: properties and applications, Biomaterials 12 (1991) 155–163.
[28] S. Wang, Z.H. Liao, Y.H. Liu, W.Q. Liu, Influence of thermal oxidation temperature on the microstructural and tribological behavior of Ti6Al4V alloy, Surf. Coat. Technol 240 (2014) 470–477.
[29] P. Zhang, Y.T. Li, Z. Chen, J.Y. Zhang, B.L. Shen, Oxidation response of a vacuum arc melted NbZrTiCrAl refractory high entropy alloy at 800-1200 °C, Vacuum 162 (2019) 20–27.
[30] J. Jayaraj, P. Thirathipviwat, J. Han, A. Gebert, Microstructure, mechanical and thermal oxidation behavior of AlNbTiZr high entropy alloy, Intermetallics 100 (2018) 9–19.
[31] C. Wagner, Theoretical analysis of the diffusion processes determining the oxidation rate of alloys, J. Electrochem. Soc. 99 (1952) 369–380.
[32] T.F. Li, High Temperature Oxidation and Hot Corrosion of Metals, Chemical Industry Press, BJ, 2003.
[33] N.B. Hua, X.S. Hong, Z.L. Liao, Q.T. Wang, L. Zhang, Q.H. Guo, X.Y. Ye, J. Brechtl, P.K. Liaw, A biocompatible Pd-based BMG with excellent corrosive-wear resistance for implant applications, Intermetallics 124 (2020), 106847.
[34] J. Joseph, N. Haghdadi, K. Shamlaye, P. Hodgson, M. Barnett, D. Fabijanic, The sliding wear behaviour of CoCrFeMnNi and $Al_xCoCrFeNi$ high entropy alloys at elevated temperatures, Wear 428-429 (2019) 32–44.
[35] H. Kato, K. Komai, Tribofilm formation and mild wear by tribo-sintering of nanometer-sized oxide particles on rubbing steel surfaces, Wear 262 (2007) 36–41.
[36] L. Huang, Z. Cao, H.M. Meyer, P.K. Liaw, E. Garlea, J.R. Dunlap, T. Zhang, W. He, Responses of bone-forming cells on pre-immersed Zr-based bulk metallic glasses: effects of composition and roughness, Acta Biomater 7 (2011) 395–405.